Vol. 45, No. 4 (2023) 634-642, DOI: 10.24874/ti.1504.06.23.09

Tribology in Industry

www.tribology.rs

RESEARCH

Effect of Internal Structure of Circular Dimples on Hydrodynamic Lubrication Characteristics of Thrust Bearings

Ryota Ishi[a], Reo Miwa[a], Norifumi Miyanaga[b,*], Jun Tomioka[c]

[a]*Graduate School of Engineering, Kanto Gakuin University, 1-50-1 Mutsuurahigashi, Yokohama, Japan,*
[b]*Faculty of Science and Engineering, Kanto Gakuin University, 1-50-1 Mutsuurahigashi, Yokohama, Japan,*
[c]*Faculty of Science and Engineering, Waseda Univerisity, 3-4-1 Okubo, Tokyo, Japan.*

Keywords:

Thrust bearings
Hydrodynamic lubrication
Dimples
Cavitation

* Corresponding author:

Norifumi Miyanaga
E-mail: miyanaga@kanto-gakuin.ac.jp

Received: 28 June 2023
Revised: 18 July 2023
Accepted: 7 September 2023

A B S T R A C T

In this study, the effects of three types of dimples with different internal structures on the fluid lubrication characteristics of seal-like thrust bearings were experimentally and numerically investigated. In the experiments, the load-carrying capacity and the frictional torque were measured. The measurements were performed with a fixed constant film thickness. The behaviors of cavitation bubbles occurred within the dimples were observed through the rotating glass plate. Three types of internal structures of dimples were tested: cylindrical, spherical and conical. The measurement results were simulated by using the Reynolds equation. In addition, applying the periodic condition, a single dimple was analyzed. As the results, in three types of dimples, the load-carrying capacity increased as the rotational speed increased. The cylindrical internal structure built up the largest pressure at the trailing edge of dimples, and consequently the largest load-carrying capacity. The frictional torque also increased with increasing the rotational speed in the dimpled bearings. However, the effect of the internal structure on the frictional torque was not significant. Analytical results showed that the pressure reached the maximum value at the trailing edge of the cylindrical internal structure. The conical and sphere internal structure had the maximum value slightly inside the trailing edge.

1. INTRODUCTION

When lubricated parallel smooth bearings with a dimple on at least one side are subjected to relative motion, oil-film pressure is generated at the dimple owing to the hydrodynamic effect. The pressure is negative at the entrance of the dimple and positive at the exit. As cavitation bubbles are generated in the negative-pressure area, the load-carrying capacity (LCC) can be obtained, and no contact can be maintained between the bearing surfaces [1]. Several other promising mechanisms for generating the LCC have been proposed [2-5]. These publications commonly

note that the ability of dimples to provide the LCC has a strong influence on the lubrication characteristics. Since the pioneering works by Etsion et al. [6], texturing has attracted attention for improving the lubrication performance of machine elements [7-14]. Many researchers attempted to provide optimal designs for fully and partially textured bearings in analysis based on the Reynolds equation or the Navier-Stokes equation [15-17]. According to published papers, the depth and the density of dimples are key factors that provide the optimum LCC [18,19].

For microtextured surfaces, it is not easy to experimentally clarify the behavior of a single dimple because of its size. Cross et al. [20,21] investigated thrust washers with larger pockets and showed the pressure map in which the cavitation region and the location of peak pressure were clearly displayed using thin-film pressure transducers. However, they did not investigate the effect of the internal structure of dimples. The effect of the internal dimple structures has not been sufficiently studied, despite its importance in determining the LCC. Notably, Cong et al. [22] experimentally and numerically studied the effect of several internal shapes of dimples on the LCC. Nanbu et al. [23] numerically studied the EHL performance of different dimple bottom shapes.

In a conventional bearing-test device, the oil-film thickness changes in different dimples for balancing with the applied load. Therefore, the experimental discussion in dimple size has included the difference in oil-film thickness according to the LCC of each dimple. To overcome this difficulty, the authors newly developed an experimental apparatus in which the frictional torque, LCC, and cavitation area ratio in the dimples could be measured while maintaining a constant oil-film thickness [24]. Using this device, the hysteresis characteristics of the LCC caused by cavitation bubbles were clarified in a previous study [25]. In addition, the measurement results using this device were compared with the experimental results under a constant load, which is considered common practice. The results were consistent with each other, thus validating the experimental method [26].

In this study, the effects of different internal dimple structures on the fluid lubrication characteristics of seal-like thrust bearings were experimentally investigated. The developed device allows for discussing the effect of the internal structure of dimples under a constant oil-film thickness and provides additional insight into the lubrication characteristics of dimpled bearings. The behavior of the cavitation bubbles in the dimples was also observed. The simple analysis using the Reynolds equation was conducted to gain the trend of the effect of the internal structure of dimples.

2. EXPERIMENTS

2.1 Experimental apparatus

Fig. 1 shows a schematic of the experimental apparatus used in this study [24-26]. The thrust bearing consists of an upper glass disk and a dimpled brass specimen.

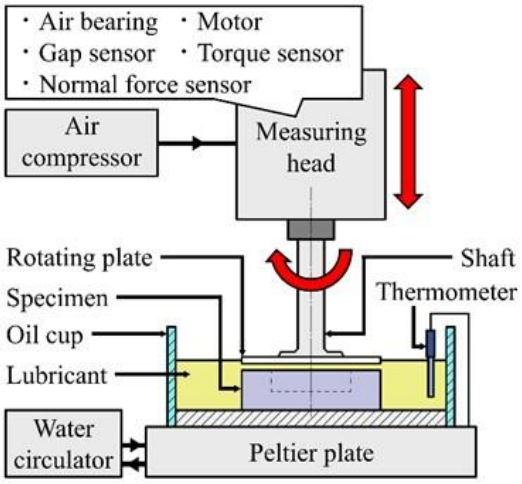

Fig. 1. Experimental apparatus.

The glass disk was rotated in unison with at rotating shaft, which was supported by an aerostatic bearing. The dimpled specimen was bolted to an oil cup. A Peltier device was built at the bottom of the oil cup to maintain a constant lubricant temperature. Unlike conventional tribometers that apply a constant load, this apparatus controls the oil-film thickness and can measure the LCC using a normal force sensor located in the measuring head. The frictional torque generated between the glass disk and the dimpled specimen was measured using a torque sensor. The lubricated surfaces were observed through the glass disk. To improve the visibility, a green laser was irradiated in the form of a sheet. A digital camera was used to record cavitation bubbles generated in the dimples.

2.2 Specimens

Fig. 2 shows a schematic of the dimpled specimens, and Fig. 3 shows the internal structures of the dimples tested in this experiment.

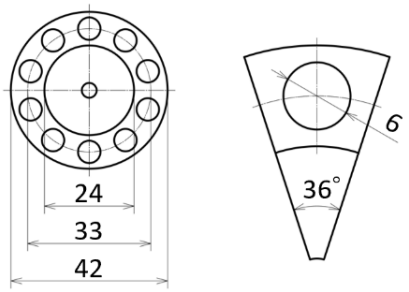

Fig. 2. Specimen and dimple dimensions.

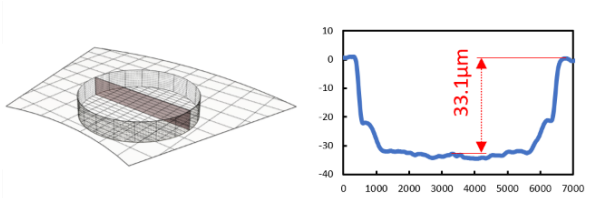

(a) Cylindrical

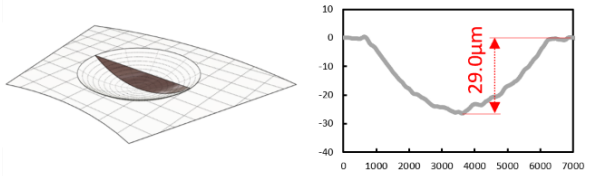

(b) Spherical

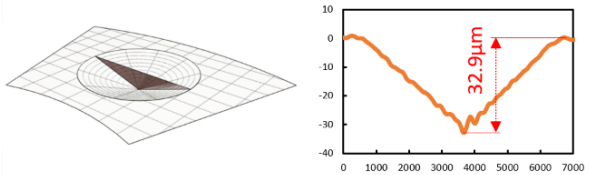

(c) Conical

Fig. 3. Measured internal dimple structures.

The inner and outer diameter of the lubricating surface were d_o=24mm and d_i=42mm, respectively. Ten dimples, each with the diameter d_d=6mm, were evenly distributed on the lubricating surface of the specimens. Three types of internal structures were tested: cylindrical, spherical and conical. Each dimple was drilled to the maximum depth of approximately δ_{max}=30μm. The area ratio of the dimple to the lubricating surface was 30%. In the side wall of the specimens, for oil replacement, a circulation hole of diameter 2mm was drilled. The hole ensured that the pressures on the inner and outer sides of the lubricating area were maintained at the atmospheric pressure.

2.3 Procedure

First, the dimpled specimen was submerged in the lubrication oil. A shaft with a glass plate was attached to the spindle located on the measuring head, as shown in Fig. 1. The film thickness was fixed at a constant value. After the temperature of the lubricating oil was maintained at a setting value, the rotational speed was increased up to 600min^{-1} in the increment of 100min^{-1}. The measurements were repeated five times and the average values were recorded. The cavitation bubbles that occurred within the dimples were captured using the digital camera. The area ratio of the bubble to the dimple was analyzed for each experimental condition. Table 1 lists the test conditions. The bulk temperature of the lubrication oil was maintained at 298±0.1K by using the Peltier device. The lubrication oil was Newtonian and its viscosity was 0.21Pa·s at 298K.

Table 1. Experimental condition.

Rotational speed, n (min^{-1})		0-600
Test period, t (s)		100
Oil-film thickness, h (μm)		30
Lubricant	Temperature, T_L (K)	298 ± 0.1
	Density, ρ (kg/m^3)	883
	Viscosity, η (Pa·s)	0.21

2.4 Numerical analysis

Simple analysis was conducted to gain the trends of frictional torque and LLC for the three types of the internal dimple structures. The dimensionless Reynolds equation, formula (1), was used for the calculations.

$$\frac{\partial}{\partial \bar{r}}\left(\bar{r}\bar{h}^3\frac{\partial \bar{p}}{\partial \bar{r}}\right)+\frac{\partial}{\partial \bar{\theta}}\left(\frac{\bar{h}^3}{\bar{r}}\frac{\partial \bar{p}}{\partial \bar{\theta}}\right)=6\bar{r}\frac{\partial \bar{h}}{\partial \bar{\theta}} \tag{1}$$

where $\bar{p}$ denotes the oil-film pressure. $\bar{h}$ was the followings for each dimple. Their distributions are shown in Fig. 4.

$$\bar{h}=\frac{h+\delta}{\delta_{max}}$$
$$\delta=\begin{cases}0 & at \quad r_d \le r_{xy}\\ \delta_{r,\vartheta} & at \quad r_d > r_{xy}\end{cases} \tag{2}$$
$$r_{xy}=\sqrt{(r\sin\vartheta)^2+(r\cos\vartheta-r_m)^2}$$

Cylindrical

$$\delta_{r,\vartheta}=\delta_{max} \tag{3}$$

Spherical

$$\delta_{r,\vartheta} = \sqrt{SR^2 - {r_{xy}}^2} - \sqrt{SR^2 - {r_d}^2} \quad \left(SR = \frac{{\delta_{max}}^2 + {r_d}^2}{2\delta_{max}}\right) \tag{4}$$

Conical

$$\delta_{r,\vartheta} = \delta_{max}\frac{r_d - r_{xy}}{r_d} \tag{5}$$

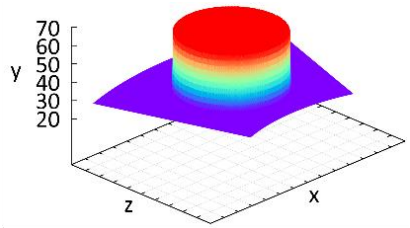

(a) Cylindrical

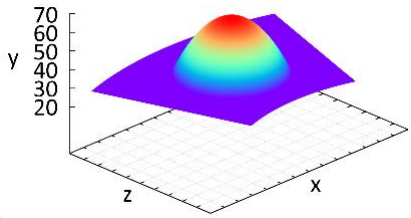

(b) Spherical

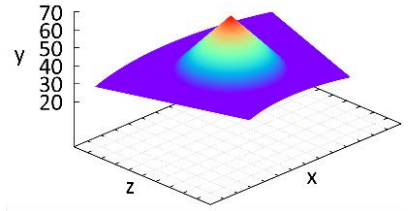

(c) Conical

Fig. 4. Oil-film distributions used in analysis.

The flow rate and velocity were calculated by Formulas (6)-(9)

$$\bar{q}_r = -\frac{\bar{h}^3}{12}\frac{\partial \bar{p}}{\partial \bar{r}} \tag{6}$$

$$\bar{q}_\theta = -\frac{\bar{h}^3}{12}\frac{\partial \bar{p}}{\partial \bar{\theta}} + \frac{\bar{r}\bar{h}}{2} \tag{7}$$

$$\bar{u}_r = \frac{(\bar{y} - \bar{h})\bar{y}}{2}\frac{\partial \bar{p}}{\partial \bar{r}} \tag{8}$$

$$\bar{u}_\theta = \frac{(\bar{y} - \bar{h})\bar{y}}{2\bar{r}}\frac{\partial \bar{p}}{\partial \bar{\theta}} + \frac{\bar{r}}{\bar{h}}(\bar{h} - \bar{y}) \tag{9}$$

The analytical model with a single dimple is shown in Fig. 5. This model corresponds to one-tenth of the bearing surface area. Many literatures have pointed out that the JFO model is better for dimple analysis, but the selection of the cavitation pressure is problematic when the cavitation in dimpled bearings is considered numerically. Therefore, many researchers made assumptions about the cavitation pressure that may not be realistic for analysis. In this study, for the purpose of simply gaining the trends of dimple behaviors, the simplest model of treatment of cavitation, the half-Sommerfeld condition, was adopted. The model was used even now in the analysis of dimpled bearings [27]. In addition, atmospheric pressure was assumed at the radial bearing ends and periodic conditions were assumed for the circumferential ends. Formula (10) presents the boundary conditions.

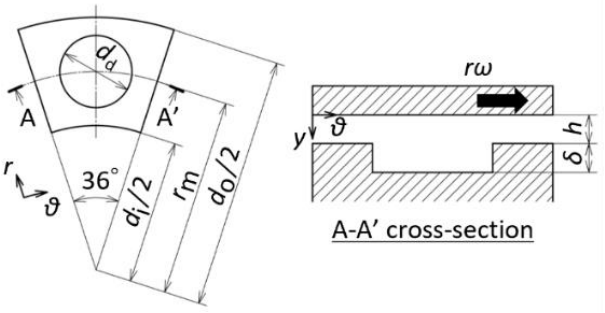

Fig. 5. Analytical model (ex. cylindrical).

$$\left.\begin{aligned} \bar{p}|_{r=r_o} &= \bar{p}|_{r=r_i} = 0 \\ \bar{p}|_{\theta=0} &= \bar{p}|_{\theta=\frac{\pi}{5}} \\ \left.\frac{\partial \bar{p}}{\partial \bar{\theta}}\right|_{\theta=0} &= \left.\frac{\partial \bar{p}}{\partial \bar{\theta}}\right|_{\theta=\frac{\pi}{5}} \\ \bar{p}|_{\bar{p}<0} &= 0 \end{aligned}\right\} \tag{10}$$

3. RESULTS AND DISCUSSION

3.1 Experimental results

Fig. 6 shows the measurement results of the frictional torque for each dimple. For the measurements, the oil-film thickness was set to h=30μm. The error bars indicate the standard deviation. The theoretical value shows the calculation result for the plane (dimple-free) bearing, which can be obtained using Formula (11).

$$T = \frac{\pi\eta\omega({r_o}^4 - {r_i}^4)}{2h} \quad (11)$$

where T is the frictional torque, h is the initially fixed oil-film thickness, η is the viscosity of the lubricant, ω is the angular velocity, r_o is the outer radius of the lubricating surface, and r_i is the inner radius of the lubricating surface. The experimental frictional torque of the plane bearing was consistent with the theoretical value, confirming that the oil-film thickness was properly controlled. The flatness of the specimen could also be considered sufficient.

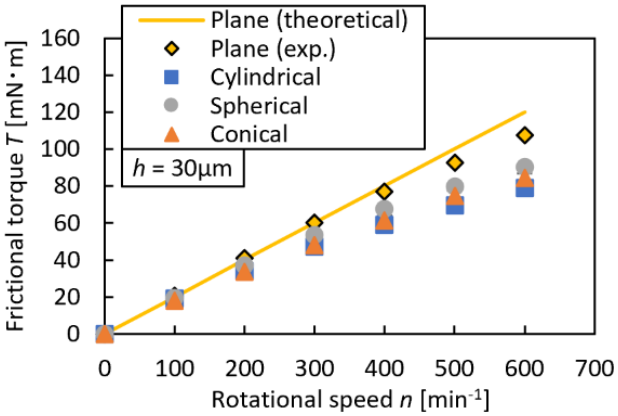

Fig. 6. Measurement results of frictional torque.

For all the dimples, the frictional torque increased with the rotational speed. The frictional torque of the dimpled bearings was lower than that of the plane bearing. However, the effect of the internal structure of the dimples was not significant. The frictional force was considered to be dominated by the ridge, which occupied 70% of the sliding surface. The cylindrical dimple demonstrated the lowest frictional torque. The average oil-film thickness h' was different for the three dimples tested in this experiment. Therefore, the frictional torque T' was calculated by using Formula (12), in which the average oil-film thickness h' was used instead of h, and the calculated frictional torques were compared with the experimental results, as shown in Fig. 7.

$$T' = \frac{\pi\eta\omega({r_o}^4 - {r_i}^4)}{2h'} \quad (12)$$

The differences between the experimental results and the theoretical values are more apparent for each internal structure of the dimples, compared with Fig. 6. This figure shows that the contribution of the internal structure of the dimple to the friction reduction is the greatest in the conical dimple, whereas in the cylindrical dimple, the effect of the increase in the average oil-film thickness is comparatively greater.

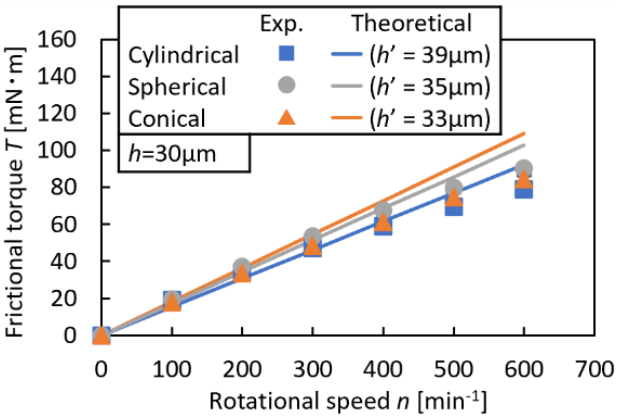

Fig. 7. Measurement results of frictional torque.

Fig. 8 shows the relationship between the LCC and the rotational speed. In this measurement, the oil-film thickness was set to h=30μm. The error bars indicate the standard deviation.

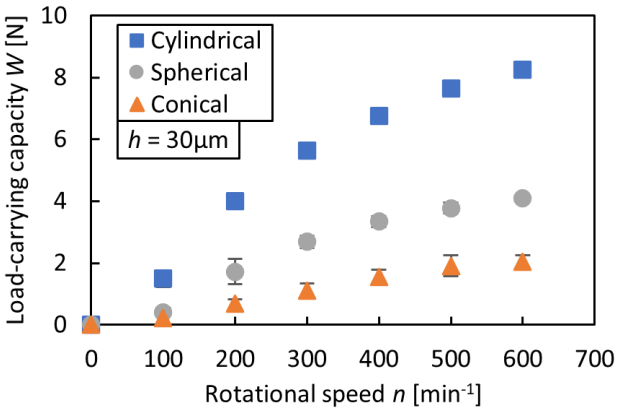

Fig. 8. Measurement results of LCC

The LCC increased with the rotational speed, regardless of the internal structure. Among the three dimples, the cylindrical dimple had the largest LCC, whereas the conical dimple had the smallest valuse. Within the scope of this study, the maximum LCC of the cylindrical dimples was approximately four times greater than that of the conical dimples. The contribution of the internal structures on the LCC was remarkable.

Fig. 9 compares the observed results for the cavitation bubbles generated in each dimple tested. The rotational speed was set to n=600 min^{-1} in this observation. The arrows indicate the rotational direction of the smooth glass disk. Cavitation bubbles were generated within these dimples. Seat-shaped bubbles were

observed in the cylindrical dimple, whereas finger-shaped bubbles were observed in the spherical and conical dimples.

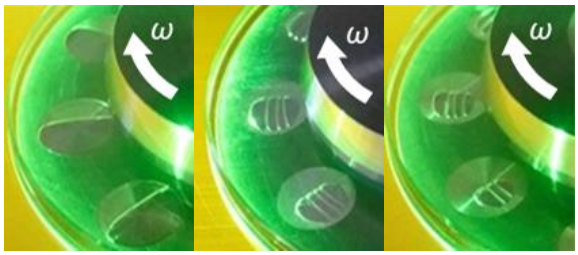

(a) Cylindrical (b) Spherical (c) Conical

Fig. 9. Cavitation bubbles in dimples (600min^{-1})

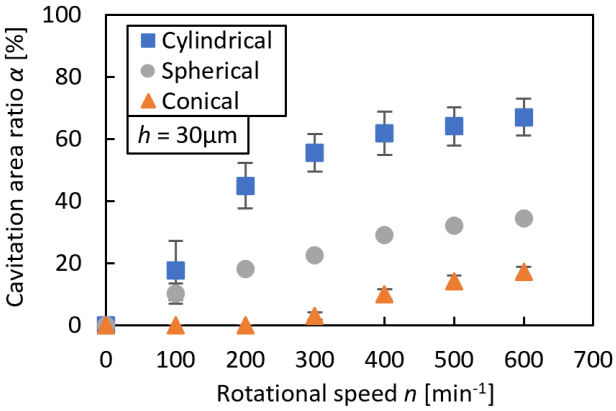

Fig. 10. Comparison of cavitation area ratios

Fig. 10 shows the results of the cavitation area ratio. The ratio α was calculated using Formula (13).

$$\alpha = \frac{A_c}{A_d} \times 100 \tag{13}$$

where A_d and A_c denote the area of the dimple and cavitation bubble, respectively. The cavitation area ratio α was the largest in the cylindrical dimple, and it reached more than 60% as the rotational speed increased. For the conical dimple, the cavitation area ratio α was small at n=100 and 200 min^{-1}, and the LCC shown in Fig. 7 was also small.

3.2 Analytical results

Fig. 11 shows the analytical pressure contours, and 2D distributions in section A-A (r=r_m) and B-B (r=r_m+Δr). The arrow indicates the direction of rotation of the smooth glass plate. The cylindrical dimple exhibited the highest pressure, whereas the conical dimple had the smallest value. These results were consistent with the experimental results, in which the cylindrical dimple had the largest LCC, whereas the conical dimple had the smallest value. The pressure reached its maximum value on the trailing edge of the cylindrical dimple but slightly inside the trailing edge in the spherical and conical dimples. In addition, in the spherical and conical dimples, the pressure peaks were not sharp compared with those in the cylindrical dimple. For the spherical and conical dimples, the wedge effect was not sufficient compared with that of the cylindrical dimple, as the dimple depth gradually decreasedas Δr increased.

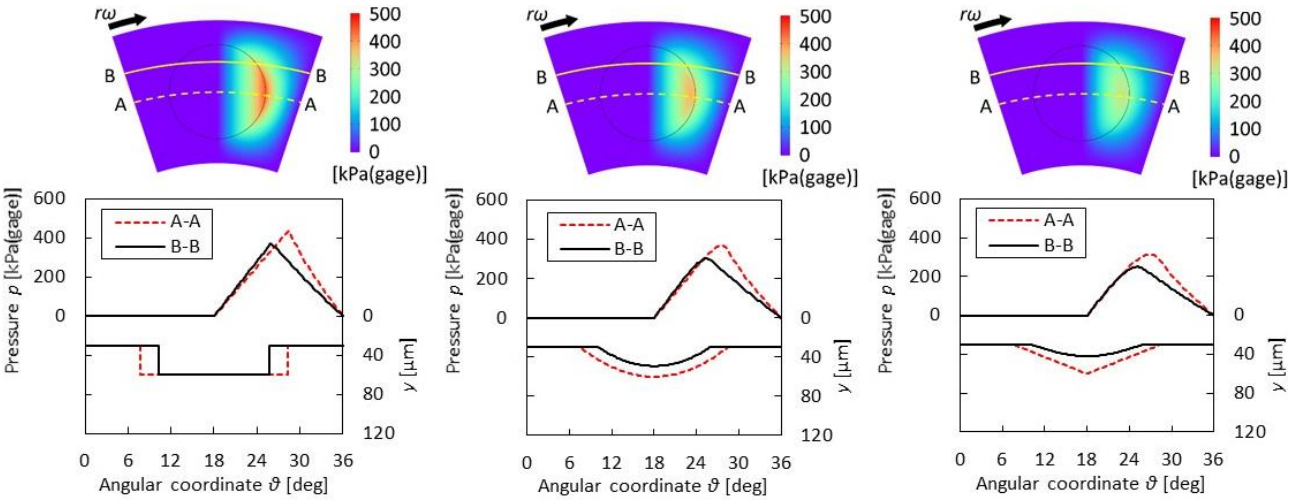

(a) Cylindrical (b) Spherical (c) Conical

Fig. 11. Analytical pressure distribution for each internal structure.

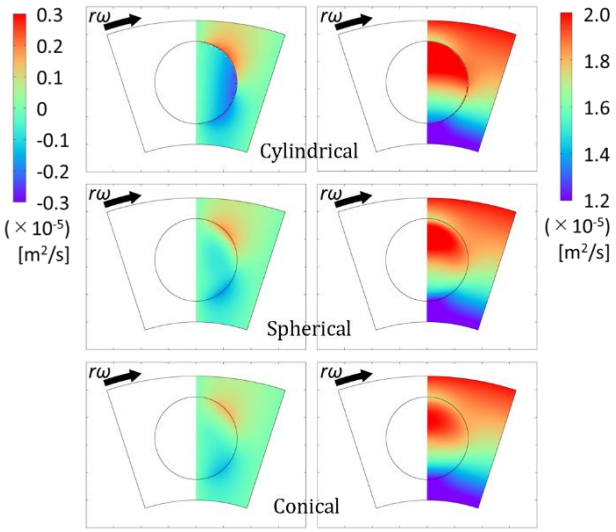

Fig. 12. Flow rate in the wedge region of the dimples.

Figs. 12(a) and 12(b) show the flow rates in the r- and θ-directions. In this analysis, the half-Sommerfeld condition was applied to the calculations, and thus the results were shown only for the wedge region. The results suggested that the lubrication oil was discharged from the inside of the dimple not only to the θ-direction but also to the r-direction. In addition, the lubricating oil remaining within the dimple flowed to the negative r-direction owing to the velocity difference. This flow was the greatest in the cylindrical dimple and the smallest in the conical dimple.

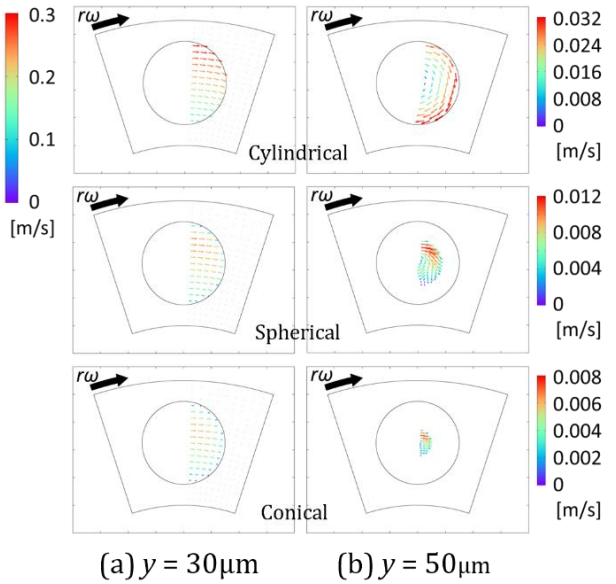

Fig. 13. Flow velocity distribution in the wedge region of the dimples.

The conical dimple is considered to have the smoothest discharge of lubricating oil, resulting in the smallest LCC. Figs. 13(a) and 13(b) show the flow velocity distribution in the dimples at y=30 and 50μm. For the cylindrical dimple, the flow velocity was higher at the outer periphery, whereas for the spherical and conical dimples, the flow velocity was slightly higher inside the edge of the dimple. At y=50μm, a swirling flow occurred along the dimple wall.

4. CONCLUSIONS

In this study, the effects of different internal dimple structures on the fluid lubrication characteristics of thrust bearings were experimentally and analytically investigated. Three types of internal structures were tested: cylindrical, spherical and conical. The results obtained were as follows.

1. The contribution of the internal structure of the dimple to the friction reduction was greater for the conical dimple, whereas for the cylindrical dimple, the effect of the increase in average oil-film thickness was comparatively greater.
2. The cylindrical dimple exhibited the largest LCC, whereas the concal dimple exhibited the smallest valuse. The maximum LCC of the cylindrical dimples was approximately four times that of the conical dimples.
3. The seat-shaped cavitation bubbles were observed in the cylindrical dimples, whereas the finger-shaped bubbles were observed in the conical and spherical dimples.
4. The analytical pressure distribution showed that, for the spherical and conical dimples, the wedge effect was insufficient compared with that for the cylindrical dimple.

REFERENCES

[1] D. Gropper, L. Wang, and T. J. Harvey, "Hydrodynamic lubrication of textured surfaces: A review of modeling techniques and key findings," *Tribology International*, vol. 94, pp. 509–529, Feb. 2016, doi: 10.1016/j.triboint.2015.10.009.

[2] K. Yagi and J. Sugimura, "Balancing wedge Action: a contribution of textured surface to hydrodynamic pressure generation," *Tribology Letters*, vol. 50, no. 3, pp. 349–364, Apr. 2013, doi: 10.1007/s11249-013-0132-z.

[3] A. D. Olver, M. Fowell, H. A. Spikes, and I. Pegg, "'Inlet suction', a load support mechanism in non-convergent, pocketed, hydrodynamic bearings," *Proceedings of the Institution of Mechanical Engineers, Part J: Journal of Engineering Tribology*, vol. 220, no. 2, pp. 105–108, Feb. 2006, doi: 10.1243/13506501jet168.

[4] K. Tønder, "Hydrodynamic effects of tailored inlet roughnesses: extended theory," *Tribology International*, vol. 37, no. 2, pp. 137–142, Feb. 2004, doi: 10.1016/s0301-679x(03)00043-4.

[5] M. B. Dobrica and M. Fillon, "About the validity of Reynolds equation and inertia effects in textured sliders of infinite width," *Proceedings of the Institution of Mechanical Engineers, Part J: Journal of Engineering Tribology*, vol. 223, no. 1, pp. 69–78, Jan. 2009, doi: 10.1243/13506501jet433.

[6] I. Etsion and L. Burstein, "A Model for Mechanical Seals with Regular Microsurface Structure," *Tribology Transactions*, vol. 39, no. 3, pp. 677–683, Jan. 1996, doi: 10.1080/10402009608983582.

[7] G. B. Gadeschi, K. Backhaus, and G. Knoll, "Numerical analysis of Laser-Textured Piston-Rings in the hydrodynamic lubrication regime," *Journal of Tribology*, vol. 134, no. 4, Sep. 2012, doi: 10.1115/1.4007347.

[8] N. Miyanaga and J. Tomioka, "Effect of support stiffness and damping on stability characteristics of herringbone-grooved aerodynamic journal bearings mounted on viscoelastic supports," *Tribology International*, vol. 100, pp. 195–203, Aug. 2016, doi: 10.1016/j.triboint.2016.01.019.

[9] N. Tala-Ighil, M. Fillon, and P. Maspeyrot, "Effect of textured area on the performances of a hydrodynamic journal bearing," *Tribology International*, vol. 44, no. 3, pp. 211–219, Mar. 2011, doi: 10.1016/j.triboint.2010.10.003.

[10] Y. Tokunaga, H. Inoue, K. Okada, T. Shimomura, and Y. Yamamoto, "Effects of cavitation ring formed on Laser-Textured surface of mechanical seal," *Tribology Online*, vol. 6, no. 1, pp. 36–39, Jan. 2011, doi: 10.2474/trol.6.36.

[11] N. Miyanaga and J. Tomioka, "Effect of Dynamic Properties of Support O-Rings on stability of Herringbone-Grooved Aerodynamic Journal bearings," *Tribology Online*, vol. 11, no. 2, pp. 272–280, Jan. 2016, doi: 10.2474/trol.11.272.

[12] J. Tomioka and N. Miyanaga, "Effect of surface roughness of mechanical seals under blood sealing," *Lubrication Science*, vol. 22, no. 10, pp. 443–452, Jun. 2010, doi: 10.1002/ls.124.

[13] Y. Wang, Y. Zhang, and R. Long, "Effect of compound pit textures on the friction and wear of thrust cylindrical roller bearings under starved lubrication," *Industrial Lubrication and Tribology*, vol. 75, no. 3, pp. 343–351, Mar. 2023, doi: 10.1108/ilt-10-2022-0307.

[14] J. Ruan, X. Wang, Y. Wang, and C. Li, "Study on Anti-Scuffing Load-Bearing thermoelastic Lubricating Properties of meshing gears with contact Interface Micro-Texture Morphology," *Journal of Tribology*, vol. 144, no. 10, May 2022, doi: 10.1115/1.4054400.

[15] N. K. Singh and R. K. Awasthi, "Influence of texture geometries on the performance parameters of hydrodynamic journal bearing," *Proceedings of the Institution of Mechanical Engineers, Part J: Journal of Engineering Tribology*, vol. 235, no. 10, pp. 2056–2072, Jan. 2021, doi: 10.1177/1350650120982691.

[16] G. Fu and A. Untăroiu, "An optimum design approach for textured thrust bearing with Elliptical-Shape dimples using computational fluid dynamics and design of experiments including cavitation," *Journal of Engineering for Gas Turbines and Power*, vol. 139, no. 9, Apr. 2017, doi: 10.1115/1.4036188.

[17] T. Chen, J. Ji, Y. Fu, P. Tian, J. Zhou, and X. Yang, "Tribological analysis of picosecond laser partially textured thrust bearings with circular grooves machined: Theory and experiment," *Proceedings of the Institution of Mechanical Engineers, Part J: Journal of Engineering Tribology*, vol. 236, no. 1, pp. 105–122, Mar. 2021, doi: 10.1177/13506501211005873.

[18] X. Wang, K. Kato, K. Adachi, and K. Aizawa, "Loads carrying capacity map for the surface texture design of SiC thrust bearing sliding in water," *Tribology International*, vol. 36, no. 3, pp. 189–197, Mar. 2003, doi: 10.1016/s0301-679x(02)00145-7.

[19] Y. Qiu and M. M. Khonsari, "Performance analysis of Full-Film textured surfaces with consideration of roughness effects," *Journal of Tribology*, vol. 133, no. 2, Mar. 2011, doi: 10.1115/1.4003303.

[20] A. T. Cross, F. Sadeghi, R. G. Rateick, and S. Rowan, "Hydrodynamic pressure generation in a pocketed thrust washer," *Tribology Transactions*, vol. 56, no. 4, pp. 652–662, Jul. 2013, doi: 10.1080/10402004.2013.777985.

[21] A. T. Cross, F. Sadeghi, L. Cao, R. G. Rateick, and S. Rowan, "Flow visualization in a pocketed thrust washer," *Tribology Transactions*, vol. 55, no. 5, pp. 571–581, Sep. 2012, doi: 10.1080/10402004.2012.681343.

[22] C. Shen and M. M. Khonsari, "Effect of Dimple's internal structure on hydrodynamic lubrication," *Tribology Letters*, vol. 52, no. 3, pp. 415–430, Oct. 2013, doi: 10.1007/s11249-013-0225-8.

[23] T. Nanbu, N. Ren, Y. Yasuda, D. Zhu, and Q. J. Wang, "Micro-Textures in concentrated Conformal-Contact lubrication: effects of texture bottom shape and surface relative motion," *Tribology Letters*, vol. 29, no. 3, pp. 241–252, Feb. 2008, doi: 10.1007/s11249-008-9302-9.

[24] N. Miyanaga, T. Kishida, and J. Tomioka, "Experimental investigation of load carrying capacity and frictional torque of dimpled parallel thrust bearings," *Journal of Advanced Mechanical Design Systems and Manufacturing*, vol. 14, no. 3, p. JAMDSM0041, Jan. 2020, doi: 10.1299/jamdsm.2020jamdsm0041.

[25] R. Miwa, N. Miyanaga, and J. Tomioka, "Appearance of Hysteresis Phenomena on Hydrodynamic Lubrication in a Seal-Type Thrust Bearing with Dimples," *Materials*, vol. 14, no. 18, p. 5222, Sep. 2021, doi: 10.3390/ma14185222.

[26] R. Miwa, N. Miyanaga, A. Tsujimori, J. Tomioka, "Investigations of lubrication characterises of dimpled seal-type thrust bearings by experiments under fixed allied load and fixed fluid film thickness conditions," *Journal of Japan Society for design engineering*, vol. 57, pp. 621-636, 2022, doi: 10.14953/jjsde.2022.2967

[27] H. Zhang, Y. Liu, M. Hafezi, M. Hua, and G. Dong, "A distribution design for circular concave textures on sectorial thrust bearing pads," *Tribology International*, vol. 149, p. 105733, Sep. 2020, doi: 10.1016/j.triboint.2019.04.017.

NOMENCLATURE

Dimensional quantities

n	rotational speed
ω	angular velocity
t	test period
h	oil-film thickness
T_L	temperature
ρ	density
η	viscosity
d_d	dimple diameter
r_o	outer radius of lubricating surface $(= d_o/2)$
r_i	inner radius of lubricating surface $(= d_i/2)$
r_m	surface mean radius $(= (r_o + r_i)/2)$
r_d	dimple radius$(= d_d/2)$
r_{xy}	distance between the center of a dimple and a calculation point
$\bar{u}$	flow velocity $(= u/r_{\mathrm{m}}\omega)$
δ	dimple depth
δ_{max}	maximum depth of dimple
SR	radius of curvature in spherical dimple
p	pressure
T	frictional torque
W	load-carrying capacity
A_c	cavitation area
A_d	dimple area
α	cavitation area ratio

Dimensionless quantities

$\bar{r},\ \bar{y}$	coordinates in bearing $(= r/r_{\mathrm{m}}, y/\delta_{\max})$
$\bar{\vartheta}$	coordinates in circumferential direction
$\bar{p}$	pressure $\left(= p\delta_{\max}{}^2/\eta\omega r_{\mathrm{m}}{}^2\right)$
$\bar{h}$	oil-film thickness $(= (h + \delta)/\delta_{\max})$
$\bar{q}$	flow rate $(= q/r_{\mathrm{m}}\omega\delta)$